JOURNAL OF COMPUTATIONAL PHYSICS **131,** 89–108 (1997)
ARTICLE NO. CP965576

A Dynamical Pseudo-Spectral Domain Decomposition Technique: Application to Viscous Compressible Flows

François Renaud and Serge Gauthier

CEA/Limeil-Valenton, 94195 Villeneuve St. Georges Cedex, France
E-mail: gauthier@limeil.cea.fr

Received February 6, 1996; revised August 13, 1996

A dynamical spectral domain decomposition method is presented. In each subdomain a transformation of coordinate is used. Both the locations of the interfaces and the parameters of the mappings are dynamically adapted by minimizing the H^2_ω-norm of the calculated solution. We show on some functions that the total norm of the Chebyshev series depends on the location of the interfaces. Moreover, there exists a minimum that defines the best location of the interface. This defines a dynamical generation of Chebyshev collocation points. This numerical method is applied on partial differential equations and it is shown that both the overall accuracy and the matching at the interfaces are improved with respect to a fixed interface calculation. This algorithm is then used for the numerical solution of the time-dependent full Navier–Stokes equations. The solution technique consists in a Fourier–Chebyshev collocation method combined with a matching method. The computational domain is decomposed into subdomains in the vertical direction. In each subdomain a coordinate transform is used and the locations of the interfaces are dynamically determined. The elliptic problems coming from the viscous terms are solved by means of the Chebyshev acceleration method. Density is matched with an upwind procedure whereas the velocities, the temperature, and the concentration are handled with the influence matrix method. Numerical examples are carried out on the compressible Kelvin–Helmholtz and Rayleigh–Taylor flows.

CONTENTS

1. INTRODUCTION

In this paper we present a dynamical pseudo-spectral domain decomposition technique for subsonic unsteady viscous compressible flows. The dependent variables are expanded on a Fourier–Chebyshev basis since we consider flows with one direction of spatial periodicity. In each subdomain of the inhomogeneous direction a coordinate transform, with one parameter, is used. The mappings used assume that the most rapid variation is located at the center of a subdomain. Both the mapping parameters and the locations of the subdomain interfaces are obtained by minimizing the H^2_ω-norm of the calculated solution. The matching of density uses a simple upwind procedure whereas the matching of velocity, temperature, and concentration is performed with a method derived from the influence matrix technique. The method is illustrated by the calculation of several unsteady Kelvin–Helmholtz flows and one Rayleigh–Taylor flow.

Numerical simulations of incompressible flows in which high accuracy is required are mainly carried out within the spectral method framework [1]. The situation is somewhat different in compressible flows where there are two different philosophies. On one hand, some authors consider that spectral methods cannot handle strong discontinuities, such as shock waves, and they prefer using high order finite difference schemes that have a spectral-like accuracy. However, difficulty in handling strong gradients or discontinuities is not a feature of spectral methods. It is rather a feature of high order methods, where the knowledge of derivatives of high order is needed. Consequently, all high order numerical schemes need a special development for handling strong discontinuities.

In view of this, applications of spectral methods to compressible flows have made some progress in last years. For homogeneous flows, Passot and Pouquet have developed a new artificial viscosity to perform supersonic compressible flow simulations in two and three dimensions [2]. For inhomogeneous flows, where polynomial expansions have to be used, several difficulties have to be overcome. Since compressible flows very frequently develop stiff and unsteady gradients, it is necessary to use a mapping to a new coordinate system.

Grosch and Orszag [3] first studied the numerical solution of problems in unbounded regions with coordinate

0021-9991/97 $25.00

transforms. They showed that these mappings are useful if the solution vanishes rapidly or approaches a constant at infinity; otherwise they are not particularly helpful. They also show, with some examples, that algebraic mappings are better than exponential ones. For bounded domains there are numerous examples in which mappings increase the accuracy.

An adaptive procedure was introduced by Bayliss and Matkowsky [4], in which a coordinate transform was chosen to minimize the weighted second Sobolev norm of the solution. The numerical method was proven to be efficient to compute steady nonaxisymmetric as well as unsteady axisymmetric flames. This technique was independently used by Guillard and Peyret [5], with the same norm—the weighted second Sobolev norm in L^2_ω— to one-dimensional premixed flame and two-dimensional plane flame and two-dimensional plane flame moving into a reactive medium. The authors display the histogram of the Chebyshev expansion of the solution, proving that spectral accuracy has been reached.

A new functional was introduced in [6]. The spectral interpolation error is bounded by the first neglected Chebyshev coefficients. The procedure is illustrated by the solution of some combustion problems.

In [7], mappings are used to solve a linear hyperbolic equation with Fourier and Chebyshev collocation methods. The solution obtained with a mapping adapted with the H^2-norm displayed much fewer oscillations than the solution without mapping. Moreover, adaptive methods based on the H^1-norm place too much weight on the steep gradient at the expense of the smooth regions. Consequently, adaptation based on minimizing the H^2-norm is preferred over adaptation based on the H^1-norm. Discontinuous functions require a special treatment, in addition to coordinate transforms.

In [8, 9], Guillard *et al.* compare three functionals: the weighted Sobolev norm introduced in [4, 5], the nonweighted norm, and the functional proposed in [6] that is an upper bound for the maximum norm of the spectral interpolation error. They found that, at least for the studied cases, the choice of a specific functional is not too critical. However, the crucial point is the actual evaluation of the functionals. They proposed three ways to perform this computation. It turns out that the best way is to transform the integral, which defines the norm, and to use a quadrature. They also found that some filtering procedure is needed. The functional versus the mapping parameter may have some high-frequency oscillations which can be removed by the filter. This numerical procedure is used to simulate temporally growing compressible mixing layers for convective Mach numbers ranging from 0.25 to 0.40 and Reynolds numbers up to 1000.

In [10], an analysis of the influence of mappings is conducted on simple examples. They show that mappings can improve the accuracy in three general ways. The transformed function varies less rapidly in the new space so it is better approximated by a polynomial. A second way is to map the region of rapid variation near the boundaries where the errors are smaller than in the middle of the domain. This property is due to the global character of the polynomial approximation [10]. Finally, the mapping can expand the region near the boundaries in such a way to get a more uniform distribution of collocation points. They conclude that the first strategy gives the better results. They also notice that changes in the differential operator, due to the mapping, do not negatively affect the conditioning of the matrices. In other words, coordinate transforms permit a reduction of the number of collocation points, for a given level of accuracy. Moreover, it is shown in [11] that preconditioned iterative procedures converge faster with a mapping. Mappings may also be used to obtain algorithms with a less restrictive stability condition [12].

However, mappings with only one parameter cannot handle several stiff gradients on the same domain. In these cases, coordinate transforms with several parameters have to be used. Such mappings have been used by Baylis *et al.* [13] who recently developed an adaptive approximation of solutions to problems with multiple layers. The mapping family they used depends on $3N - 1$ free parameters, where N is the number of the layers. The parameters can be determined adaptively by minimizing a functional of the calculated solution. On the other hand, multiple gradients may be handled by a multidomain strategy with a coordinate transform in each subdomain [14]. Moreover, multidomain strategy allows one to simulate flows in complicated geometries and to use parallelism techniques. Finally, compressible flows generate quasi-discontinuities and special methods have to be used. Recently, some solution techniques have been proposed in the framework of special methods [15–17].

An adaptive multidomain method has been developed in [18]. It is shown that for time-dependent solutions, fixed locations of the interfaces can degrade the accuracy. In this numerical technique, the locations of the interfaces are determined so as to minimize the maximum error in all of the subdomains, or to equalize the errors within the subdomains. In each subdomain, there is no transformation of coordinate and the Gauss–Lobatto points are used. The method is tested against a hyperbolic system. Two and three subdomain calculations are displayed. Moreover, they found that only a crude equalization is enough to obtain improvements over single domain and fixed interface multidomain calculations. An adaptive method based on different grounds has been developed in [19].

The domain decomposition strategy may be used in two ways. First, one defines a large number of subdomains, with a small number of collocation points, without mapping. This is the weak formulation, or variational formula-

tion, approach such as the spectral element method [20]. On the other hand, the strong formulation uses a relatively small number of subdomains with a large number of collocation points. Coordinate transforms are then necessary and they depend on one or more parameters.

In incompressible flows nonlinearities are only quadratic, as opposed to the compressible flows where all orders of nonlinearities are present through the density. Higher order nonlinearities become relevant as the density fluctuations are increasing. They induce couplings between Fourier modes that are usually stronger than in the corresponding incompressible flow [21]. As a result, compressible flows usually require more sophisticated numerical methods. To this end, one can distinguish several levels of complexity on the kind of flows simulated in this paper. Steady subsonic compressible flows such as the Rayleigh–Bénard instability do not require sophisticated methods [22]. Steady supersonic flows such as the supersonic boundary layer require more sophisticated numerical methods. The unsteady subsonic flows such as the Kelvin–Helmholtz or the Rayleigh–Taylor flows, where strong gradients are present, require a specific treatment. This unsteady character leads to adaptive methods. Finally, the unsteady transonic and supersonic flows would also require the treatment of shock waves in an adaptive manner. In this paper, we restrict outselves to unsteady subsonic flows [23, 24].

The remainder of this paper is organized as follows. In Section 2 we describe the one-dimensional pseudo-spectral dynamical domain decomposition method. This numerical technique is applied to the full Navier–Stokes equations in Section 3. The next section is devoted to the application of this numerical method to the Kelvin–Helmholtz and Rayleigh–Taylor flows.

2. THE ADAPTIVE PROCEDURE WITH MULTIDOMAIN

It is now well known that functions that exhibit large gradients are better interpolated with a coordinate transform [4–6, 9, 25]. In recent years, adaptive methods have been developed. They use some functionals of the calculated solution as an error bound. Several functionals have been tested and, as already stated, there is a consensus that the H^2_ω-norm of the calculated solution gives good results. A better approach is to use adaptive methods combined with a domain decomposition technique. One conclusion of the studies carried out on domain decomposition techniques is that better results may be obtained, provided the subdomain interfaces are close to their best locations. These interface locations are usually adjusted by hand. We show in this section that the criterion based on the minimum of the H^2_ω-norm may also be used to determine the best location of the subdomain interface. In other words, the sum of the norms over the number of subdomains does depend on the interface locations. We first recall the basic of the adaptive procedure in a single domain. Let $u(x_2)$ be a function defined in the interval $[x_{2,\inf}, x_{2,\sup}]$. Its Chebyshev expansion reads

$$u_N(x_2) = \sum_{k=0}^{N} a_k T_k(\xi), \tag{1}$$

where ξ belongs to the computational space. Such an expansion is valid for smooth functions u. In general a polynomial expansion is not appropriate for functions exhibiting very rapid spatial variations. In these cases, it is necessary to use a coordinate transform to bring more collocation points in the vicinity of the gradient. Such a mapping is denoted

$$x_2 = f(\mathbf{a}, \xi), \tag{2}$$

where **a** is the parameter of the mapping. For time-dependent problems, the parameter mapping has to vary. Let **b** be the new value of this parameter. It defines a new computational space by $x_2 = f(\mathbf{b}, \eta)$. The ξ and η coordinate systems are related by $\eta = \phi(\xi) = f^{-1}(\mathbf{b}, f(\mathbf{a}, \xi))$. The value of the mapping parameter **b** is chosen in such a way that u has a smooth representation. This is achieved by minimizing some functional of the variable u. The functional used in [9] is based on the inequality

THEOREM 1. *For any σ and μ such that $1 \le \mu \le \sigma$, there exists a constant C such that*

$$\|u - P_N(u)\|_{\mu,\omega} \le C(\sigma) N^{2\mu-\sigma-1/2} \|u\|_{\sigma,\omega}, \tag{3}$$

where

$$\|u\|^2_{\sigma,\omega} = \sum_{i=0}^{\sigma} \int_{-1}^{1} \left| \frac{d^i u}{d\xi^i} \right|^2 \omega(\xi)\, d\xi \quad \text{with } \omega(\xi) = 1/\sqrt{1-\xi^2}.$$

It means that the projection error in the H^σ_ω Sobolev space is bounded by the norm of the function $\|u\|_{\sigma,\omega}$. Many functionals may be built from inequality (3). The choice $\sigma = 1$, 2, and 3 has been tested. The value $\sigma = 1$ does not give good results [4, 5, 7]. Guillard *et al.* [9] found that the value $\sigma = 3$ gives results very closed to the $\sigma = 2$ case. They also found that the actual computation of the functional $J_{2,\omega}(u) = \|u\|_{2,\omega}$ is crucial. The best way to compute the functional $J_{2,\omega}(u)$ is to transform the integral in the current ξ-coordinate since the function $u_N(\xi)$ is known at the Gauss–Lobatto points. The authors also observe that the norm of the solution may be replaced by the norm of its derivative. Following this remark, we may consider rather the functional based on $\|du/d\xi\|_{\sigma-1,\omega}$. In multidomain

configurations with M subdomains, the total norm is evaluated as

$$J_2(u) = \sum_{m=1}^{M} J^m_{2,\omega}(u^m), \tag{4}$$

with

$$J^m_{2,\omega}(u^m) = \left\| \frac{du^m}{d\xi} \right\|_{1,\omega},$$

where M is the total number of subdomains and u^m the restriction of the function u to the mth subdomain. In each subdomain the parameter of the coordinate transform is adapted by the procedure above described. As we shall show in the next paragraphs, the norm over a subdomain, and consequently, the total norm depends on the location of the interfaces. In other words the total norm may be minimized by two different ways. The first one is the adaptation of the parameter mapping whereas the second way is the choice of the locations of the interfaces. This provides a criterion to determine such locations. A simple and robust procedure have been used to locate the best value of the interfaces. The algorithm may be summarized in the following way:

1. Select the interface located at $x^{m,\text{old}}_{2,\text{interface}}$, $m = 1, ..., M - 1$.

2. The best location of the interface is searched in a set of discrete values given by

$$x^m_{2,\text{interface}}(i) = (x^{m,\text{old}}_{2,\text{interface}} - \Delta X_2/2) + \frac{i-1}{N_g - 1}\Delta X_2$$
$$(i = 1, ..., N_g)$$

where ΔX_2 is the length of the interval in which the interface is allowed to move and N_g is the number of discrete values. It is usually equal to 10.

3. For each value of $x^m_{2,\text{interface}}(i)$ $(i = 1, ..., N_g)$, the following steps are carried out:

—For each subdomain, the best value of the parameter of the coordinate transform is determined by minimizing the $J^m_{2,\omega}$-norm $(m = 1, ..., M)$.

—The total norm J_2 is computed with Eq. (4). As a result, a set of N_g values of the total norm J_2: $\{J^i_2(u);\ i = 1, ..., N_g\}$ has been obtained.

4. The minimum value of the set $\{J^i_2(u);\ i = 1, ..., N_g\}$ determines the best location of the interface.

5. Select the next interface and repeat steps from 2 to 4.

6. After all interfaces have been processed, a set of Chebyshev collocation points has been defined for each subdomain. However, the best location of the interface number m has been searched while the other ones were kept fixed. Consequently, the entire procedure has to be iterated until convergence of the locations of the interfaces.

After convergence, a new set of Chebyshev collocation points has been defined in the x_2-direction. The number of iterations depends upon the number of subdomains. However, it turns out that four or five iterations are usually enough to achieve convergence. The solution is then interpolated on this new set of collocation points. In some configurations, for example, for a constant function over a subdomain the procedure above described automatically decreases the size of the subdomain without a lower bound. This defect is eliminated by imposing a lower bound for the size of each subdomain.

2.1. *Example of Functions*

Since the algorithm above described is based on the evolution of the total norm J_2 as the interface location is varied, we illustrate this behavior on two functions. First we deal with the hyperbolic tangent function. Such a function is symmetric with respect to zero, as a result the interface locations are constrained to be symmetric with respect to zero. Step 3 of the algorithm is carried out on the function

$$u(x_2) = \tanh 2x_2 \quad \text{for } -25 \le x_2 \le 25. \tag{5}$$

The Chebyshev approximation of this function has been computed for two initial distributions of subdomains. Three subdomains have been used in both cases. In the first distribution the subdomain interfaces are located at $x_2 = \pm 5$ whereas in the second one the interfaces are located at $x_2 = \pm 1$. Each subdomain is mapped in the interval $[-1, 1]$ by using the following transformation of coordinate which depends on one real positive parameter **a**

$$x_2(\zeta) = x_{2,\text{ave}} + \mathbf{a}\zeta(1 + b^2 - \zeta^2)^{-1/2},$$
$$x_{2,\text{inf}} \le x_2 \le x_{2,\text{sup}};\ -1 \le \zeta \le 1, \tag{6}$$

where $x_{2,\text{ave}} = (x_{2,\text{inf}} + x_{2,\text{sup}})/2$ and the constant b is defined by $b = 2\mathbf{a}/(x_{2,\text{sup}} - x_{2,\text{inf}})$. The parameter **a** is determined by minimizing the H^2_ω-norm of the calculated solution. Mapping (6) has been chosen here because it will be used in the solution of the full Navier–Stokes equations reported below.

Figure 1 shows the evolution of the norms of the inner and outer subdomains as well as the total norm versus the interface location $\pm x_{2,\text{interface}}$. These results have been obtained with 51 Chebyshev polynomials in each subdomain. Since the best location of the interfaces are not known at the beginning of the computation, the same num-

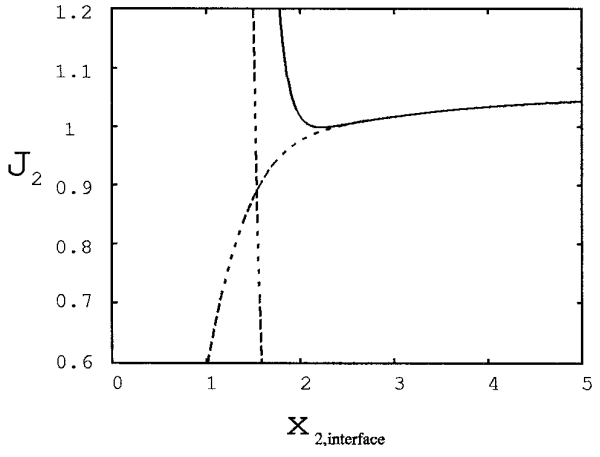

FIG. 1. The norm of the approximation of the function tanh $2x_2$ versus the location of the interface in a three-subdomain calculation. The number of collocation points is 51 in each subdomain. The interfaces are initially located at ± 5. The norms of the function in the outer and inner subdomains are given by the dashed line. The solid line stands for the total norm. The norm of the inner subdomain reaches an asymptote as the location of the interface goes away from the origin. The total norm exhibits a minimum at $x_{2,\text{interface}} = 2.05$.

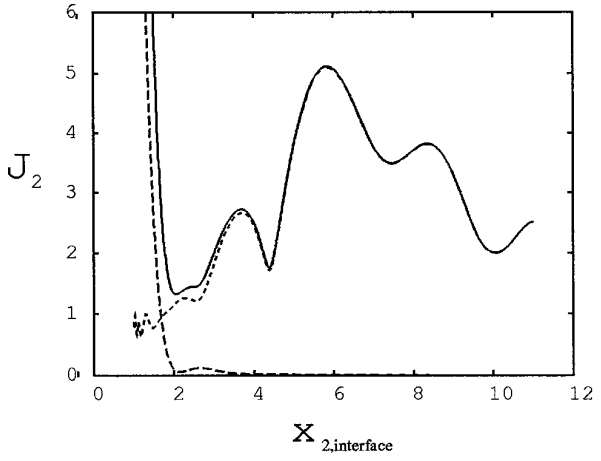

FIG. 2. Same as in Fig. 1, except that the number of collocation points is 21 and the interfaces are initially located at ± 1. The best location of the interface is also at $x_{2,\text{interface}} \simeq 2.05$.

ber of Chebyshev polynomials have been used in each subdomain, $N_1 = N_2 = N_3 = 51$. The total norm exhibits a minimum which determines the best location of the interface. The norm of the outer subdomain becomes very large as the interface location $x_{2,\text{interface}}$ goes to zero. This is related to the mapping (6) which brings collocation points in the middle of the subdomain. The norm of the function in the inner subdomain reaches an asymptotic value as $x_{2,\text{interface}}$ is larger than 2. From this value the function u is almost constant. Of course, other mappings would give different results. The second distribution of subdomains, in which $x_{2,\text{interface}} = 1$ with $N_1 = N_2 = N_3 = 51$, leads to the same curves and they are not presented here. This is no longer true for a smaller number of collocation points $N_1 = N_2 = N_3 = 21$. In this case, the first distribution of subdomains, where the interfaces are located at ± 5, gives the same curves as the one displayed in Fig. 1. However, the second distribution of subdomains, with the interfaces located at ± 1, gives a completely different behavior for the norm of the inner subdomain and the total norm as the location of the interface is varied (see Fig. 2). This may be understood by looking at Fig. 1 which shows that the first distribution ($x_{2,\text{interface}} = 5$) leads to a much smaller value of the total norm $J_{2,\omega}$ than the second distribution ($x_{2,\text{interface}} = 1$). As a result, interpolating function (5) from the first distribution to another one with a larger inner subdomain give smaller errors than the same interpolation carried out from the second distribution. This explains the large values of the total norm $J_{2,\omega}$ for large size of the inner subdomain as one can see in Fig. 2. However, the best location of the interface is also at $x_{2,\text{interface}} \simeq 2.05$. In other words, the norms of the calculated solution do depend on the initial location of the interface. It is of interest to note that there are several minima. Looking for the absolute minimum requires to search the best location in the whole domain.

As a second test we study the representation of the function $\sin x_2/x_2$. Results are displayed in Fig. 3. Three subdomains are used with 51 Chebyshev polynomials in each subdomain. The interfaces are initially located at ± 6. Since the function is more complicated with a large number of oscillations, the evolution of the norms with respect to the location of the interface is also more complicated. The norm of the function restricted to the inner subdomain

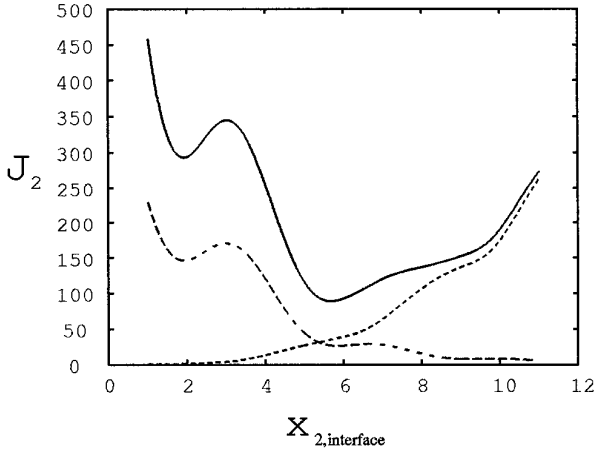

FIG. 3. Same as in Fig. 1 for the function $\sin x_2/x_2$. The number of collocation points is 51 in each subdomain and the interfaces are initially located at ± 6. The total norm exhibits a minimum at $x_{2,\text{interface}} \simeq 5.70$.

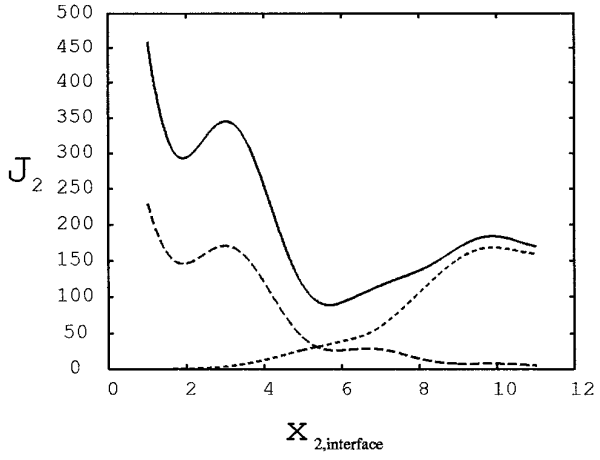

FIG. 4. Same as in Fig. 3. The number of collocation points is 51 in each subdomain and the interfaces are initially located at ±1. The total norm exhibits a minimum also at $x_{2,\text{interface}} \simeq 5.70$.

grows as the size of this subdomain increases whereas the norm associated to the outer subdomain decreases. As a result, there is a minimum located at $x_{2,\text{interface}} \simeq 5.70$. In a second numerical experiment the results of which are displayed in Fig. 4, the interfaces were placed at ±1, very far from the best value previously obtained. The number of collocation points is $N_1 = N_2 = N_3 = 51$. The procedure gives the same value for the minimum, i.e., $x_{2,\text{interface}} \simeq 5.70$. However, for very large inner subdomain, the behavior is quite different from the previous case. As for the hyperbolic tangent function, there is a strong influence of the initial distribution of the interfaces. The third numerical experiment carried out on the function $\sin x_2/x_2$ with $N_1 = N_2 = N_3 = 21$ Chebyshev polynomials is reported in Fig.

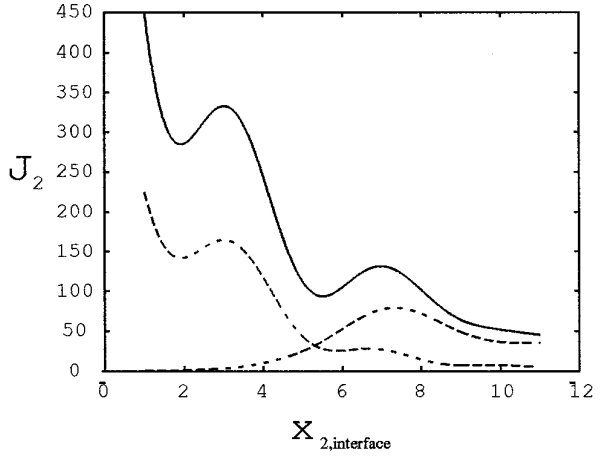

FIG. 5. Same as in Fig. 3. The number of collocation points is 21 in each subdomain and the interfaces are initially located at ±1. There is no absolute minimum.

TABLE I

Mean Value of the Errors, Defined by Eq. (12), between the Exact and the Computed Solutions for the Diffusion Equation at Time $t = 10$

$x_{2,\text{interface}}$	Interfaces	u	u'	u''	u'''
±5	Fixed	0.18×10^{-4}	0.10×10^{0}	0.13×10^{0}	0.18×10^{0}
±1	Fixed	0.34×10^{-5}	0.16×10^{-3}	0.19×10^{-3}	0.16×10^{-2}
±5	Adapted	0.16×10^{-4}	0.24×10^{-1}	0.33×10^{-1}	0.58×10^{-1}
±1	Adapted	0.13×10^{-4}	0.21×10^{-2}	0.24×10^{-2}	0.46×10^{-2}

Note. Two initial distributions of subdomains have been used. The first two runs use fixed interfaces whereas the two last ones use the dynamical generation of collocation points.

5. It does not give an absolute minimum. The smaller the number of collocation points, the stronger the influence of the initial interface distribution.

2.2. *Example of Differential Equations*

The dynamical generation of Chebyshev collocation points above described is now applied to two partial differential equations. The first example is the following one-dimensional diffusion equation

$$\frac{\partial c}{\partial t} = \frac{1}{16}\frac{\partial^2 c}{\partial x_2^2}, \quad -25 \le x_2 \le 25, \tag{7}$$

with the boundary conditions

$$\frac{\partial c}{\partial x_2}(x_2, t) = 0 \quad \text{for } x_2 = \pm 25. \tag{8}$$

Recall that the self-similar solution of Eq. (7) is

$$c_{\text{exact}}(x_2, t) = \frac{1}{2}\left(3 + \text{erf}\left(2\frac{x_2}{\sqrt{t}}\right)\right), \tag{9}$$

which allows us to define a thickness of the gradient by

$$\delta_c = x_{2,+} - x_{2,-} \quad \text{with} \left|\frac{\partial c_{\text{exact}}}{\partial x_2}(x_{2,\pm})\right| = 10^{-4}. \tag{10}$$

The initial condition is chosen to be

$$c(x_2, t = 0) = \tfrac{1}{2}(3 + \tanh 60x_2). \tag{11}$$

The diffusion equation (7) has been integrated, with a three stage low storage Runge–Kutta scheme, from time $t = 0$ to $t = 10$. Four simulations have been carried out with three subdomains and with 51 Chebyshev polynomials in each subdomain. Since the function is symmetric with respect to the origin, the interfaces are constrained to be also symmetric. Two initial distributions of subdomains have been used as shown in Tables I and II. The two last

simulations use the dynamical procedure to find the best location of the interfaces. In all cases the mapping parameters of the subdomains are adapted. A global error indicator based on the discrepancy between the exact and the computed solution has been defined. It reads

$$\mathrm{Err}[c] = \frac{1}{N}\sum_{j=1}^{N}\left|\frac{c(x_{2,j}) - c_{\mathrm{exact}}(x_{2,j})}{c_{\mathrm{exact}}(x_{2,j})}\right|, \quad \text{where } N = \sum_{m=1}^{M} N_m. \tag{12}$$

A local error indicator has also been used. It is based on the discrepancy of the solution and its derivatives on each side of the interface. It reads

$$\mathrm{ERR}[c^{(n)}] = \left|\frac{c_m^{(n)}(x_{2,m}) - c_{m+1}^{(n)}(x_{2,m})}{c_m^{(n)}(x_{2,m}) + c_{m+1}^{(n)}(x_{2,m})}\right| \quad \text{for } m = 1, ..., M-1, \tag{13}$$

where n is the order of the derivative and m the number of the subdomain. Without the dynamical adaptation of the locations of the interfaces, the data of Tables I and II show that that the results are very sensitive to the location of the subdomain interfaces. However, the best results are obtained for fixed interfaces located at ± 1. In this case, at time $t = 10$ the solution of Eq. (7) is almost a straight line between the two points $x_2 = \pm 1$. This explains why the mean value of the error is very small and the matching of the function and its derivatives are very good. It turns out that the dynamical procedure leads to very good results for two different initial locations of the interface. From Fig. 6 it also clear that the interface follows the gradient, defined by Eq. (10). Of course, a different definition would have led to a different thickness, but the important point is that both the thickness and the interface evolve in the same way. The jumps of the first derivatives are nonzero

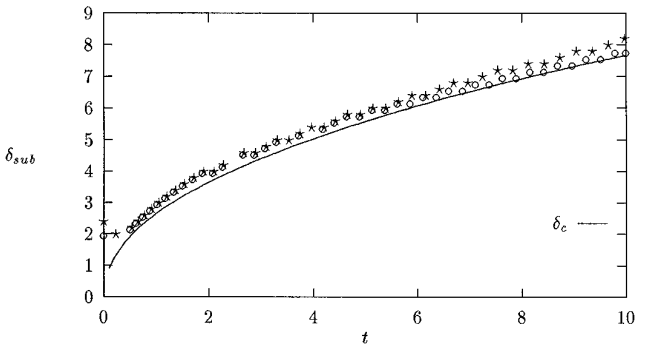

FIG. 6. Thickness, defined by Eq. (10), of the gradient of the solution of the diffusion equation (7), compared with the size of the inner subdomain in a three-subdomain calculation. The symbols ○ and ★ denote the size of the inner subdomain, δ_{sub}, between two interfaces initially located at ± 5 and ± 1, respectively. The thickness of the gradient is δ_c.

TABLE II

The Local Error of Matching of the Function and Its Derivatives between Two Subdomains, such as Defined by Eq. (13) for the Same Simulations as in Table I

$x_{2,\mathrm{interface}}$	Interfaces	u	u'	u''	u'''
±5	Fixed	0.00	0.59×10^{-7}	0.94×10^{-1}	0.95×10^{-1}
		0.00	0.44×10^{-7}	0.94×10^{-1}	0.94×10^{-1}
±1	Fixed	0.00	0.14×10^{-10}	0.54×10^{-6}	0.63×10^{-3}
		0.00	0.73×10^{-11}	0.42×10^{-6}	0.65×10^{-3}
±5	Adapted	0.00	0.49×10^{-8}	0.59×10^{-6}	0.31×10^{-4}
		0.00	0.13×10^{-8}	0.17×10^{-5}	0.83×10^{-5}
±1	Adapted	0.00	0.22×10^{-8}	0.54×10^{-5}	0.11×10^{-3}
		0.00	0.47×10^{-8}	0.56×10^{-5}	0.95×10^{-4}

Note. The upper line refers to the interface between subdomains 1 and 2. The lower one is for the interface between subdomains 2 and 3.

because the influence matrix method is a local matching procedure. The quantities reported in the fourth column of Table II are computed from spectral derivatives of the variables calculated *a posteriori.* The adaptive procedure improves the accuracy even though, for some initial distributions, the interfaces are far away their best locations. This improvement is dramatic for the jump of the second derivative; there are 5 or 6 orders of magnitude between the results with adaptive interfaces and with fixed interfaces for the ± 5 initial location of the interface. In the same way the jump of the third derivative is improved by 3 or 4 orders of magnitude. This is a noteworthy result since there is no matching condition for these derivatives.

The second and last example with partial differential equation is given by the following advection–diffusion equation

$$\frac{\partial c}{\partial t} + v(x_2, t)\frac{\partial c}{\partial x_2} = \frac{1}{\mathrm{Re}}\frac{\partial^2 c}{\partial x_2^2}, \qquad -25 \le x_2 \le 25, \tag{14}$$

where Re is a parameter. The boundary conditions are

$$\frac{\partial c}{\partial x_2}(x_2, t) = 0 \quad \text{at } x_2 = \pm 25. \tag{15}$$

The velocity v is a given function of space x_2 and time t which reads

$$v(x_2, t) = \cos t - \tanh\left(\frac{\mathrm{Re}}{2}x_2 - \frac{\mathrm{Re}}{2}\sin t\right). \tag{16}$$

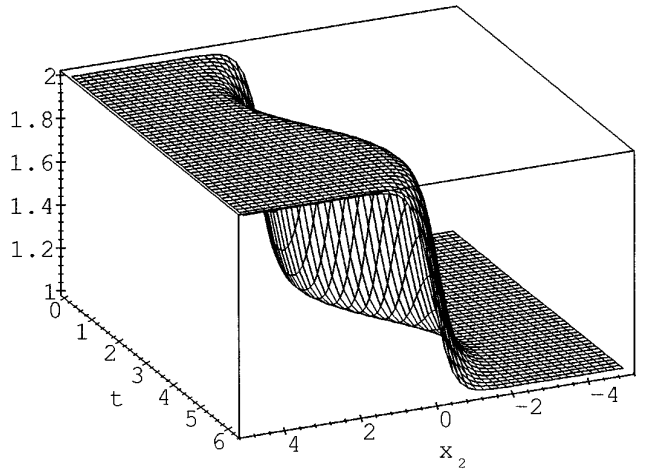

FIG. 7. Solution, c_{exact} given by Eq. (17), of the advection–diffusion equation defined by Eq. (14) in the (x_2, t) space for a parameter Re = 4.

The exact solution is

$$c_{\text{exact}}(x_2, t) = \left(3 + \tanh\left(\frac{\text{Re}}{2}x_2 - \frac{\text{Re}}{2}\sin t\right)\right)\Big/ 2. \quad (17)$$

This function with a parameter value Re = 4 is displayed in Fig. 7. The numerical solution uses the initial condition

$$c(x_2, t = 0) = \left(3 + \tanh\frac{\text{Re}}{2}x_2\right)\Big/ 2. \quad (18)$$

Equation (14) has been solved from time $t = 0$ to $t = 4$ with three initial distributions of subdomains and with the parameter Re = 4. We have used 51 Chebyshev polynomials in each subdomain. The interfaces have been located at $x_2 = \pm 4, \pm 2, \pm 1$ successively. The three first simulations keep the interfaces fixed whereas the three last ones use the moving interface procedure. The results are presented in Tables III and IV. For fixed interfaces, they are very sensitive to the location of the interfaces even though the parameter mappings of the three subdomains are adapted with the H^2_ω-norm. The choice $x_{2,\text{interface}} = \pm 4$ gives good results while the choice $x_{2,\text{interface}} = \pm 2$ corresponding to the second row of Table III gives worse results. In the third simulation ($x_{2,\text{interface}} = \pm 1$) the calculation simply blows up because adapting the mapping parameter is not efficient enough to follow the gradient through the inner subdomain.

TABLE III

Mean Value of the Errors, defined by Eq. (12), between the Exact Solution and the Computed Solution for the Advection–Diffusion Equation (14) with a Parameter Value Re = 4

$x_{2,\text{interfaces}}$	Interfaces	u	u'	u''	u'''
±4	Fixed	0.64×10^{-5}	0.43×10^{-2}	0.15×10^{-1}	0.65×10^{0}
±2	Fixed	0.19×10^{-3}	0.57×10^{0}	0.74×10^{0}	0.17×10^{1}
±1	Fixed	No sol.	No sol.	No sol.	No sol.
±4	Adapted	0.39×10^{-4}	0.86×10^{-3}	0.16×10^{-2}	0.35×10^{-2}
±2	Adapted	0.39×10^{-4}	0.86×10^{-3}	0.16×10^{-2}	0.34×10^{-2}
±1	Adapted	0.39×10^{-4}	0.50×10^{-2}	0.57×10^{-2}	0.15×10^{-1}

Note. Three initial distributions of subdomains have been used. The first three lines use fixed interfaces whereas the three last ones use the dynamical generation of collocation points. With the third distribution of subdomains with fixed interfaces, one cannot get a solution.

TABLE IV

Same Simulations as in Table III but for the Local Error, ERR, Defined by Eq. (13)

$x_{2,\text{interface}}$	Interfaces	u	u'	u''	u'''
±4	Fixed	0.00	0.51×10^{-8}	0.26×10^{-2}	0.13×10^{-1}
		0.00	*	*	*
±2	Fixed	0.00	0.17×10^{-9}	0.28×10^{-5}	0.43×10^{-4}
		0.00	0.11×10^{-6}	0.34×10^{-4}	0.33×10^{-3}
±1	Fixed	No sol.	No sol.	No sol.	No sol.
		No sol.	No sol.	No sol.	No sol.
±4	Adapted	0.00	0.49×10^{-7}	0.85×10^{-3}	0.56×10^{-2}
		0.00	0.70×10^{-5}	0.36×10^{-2}	0.51×10^{-1}
±2	Adapted	0.00	0.60×10^{-7}	0.88×10^{-3}	0.55×10^{-2}
		0.00	0.31×10^{-5}	0.35×10^{-2}	0.50×10^{-1}
±1	Adapted	0.00	0.13×10^{-7}	0.14×10^{-3}	0.43×10^{-3}
		0.00	0.69×10^{-7}	0.37×10^{-4}	0.40×10^{-2}

Note. It characterizes the jumps of the function and its derivatives between two subdomains. The upper line refers to the interface between subdomains 1 and 2. The lower one refers to the interface between subdomains 2 and 3. The symbol * means that the derivatives are too small to have significance.

With the moving interface procedure, the subdomain follows the gradient as it is shown in Fig. 8, for a parameter value Re = 4, and for three initial locations of the interfaces ±4, ±2, and ±1. In this case, the global accuracy defined by Eq. (12) depends slightly on the initial location of the interfaces. For such a parameter value, the jumps of the second derivatives are fairly small. As in the previous examples, the dynamical generation of collocation points improves the accuracy. This improvement is dramatic for the third simulation; we obtain the true solution with the same accuracy than the previous ones, although the interfaces were initially located at ±1. Indeed, since the interfaces, in the three last simulations are allowed to move with the H^2_ω criterion, the errors are fairly close.

For a parameter value 10 times larger, Re = 40, the gradient is much larger but the numerical procedure is able to follow the structure. In this simulation 51 collocation points are used in each subdomain. Results are presented in Fig. 9, where the evolution of the center of the inner subdomain, the size of the subdomain, and the thickness of the gradient are represented. The global accuracy, as

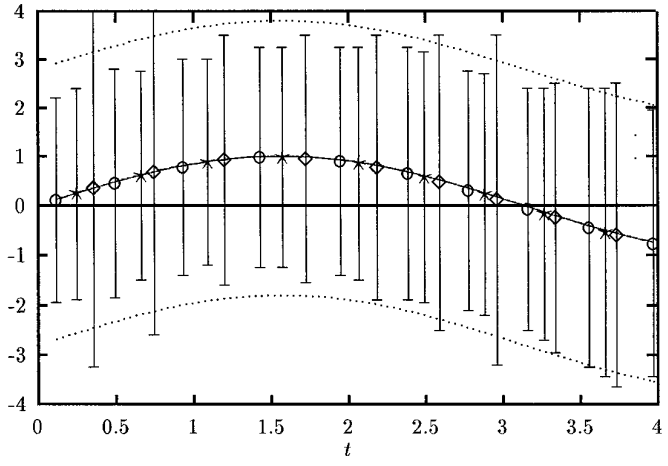

FIG. 8. Results of the solution of the advection–diffusion equation (14) with a parameter value Re = 4. Shown are the evolution of the gradient thickness in dashed lines, the center of the inner subdomain for three different initial conditions ±1, ±2, and ±4—symbols ○, ★, and ◇, respectively—and the vertical bars stand for the size of the inner subdomain. The continuous line stands for the middle of the gradient.

well as the local errors, is larger than in the previous case, as shown by data of Tables V and VI.

3. THE SPECTRAL ALGORITHM

The procedure of dynamical generation of collocation points is now applied to the full Navier–Stokes equations. The basic equations are first recalled and then the domain decomposition algorithm is detailed. The solution technique consists in a Fourier–Chebyshev method combined with a matching method. The computational domain is decomposed into subdomains in the nonperiodical direction only. In each subdomain the coordinate transform (6) is used.

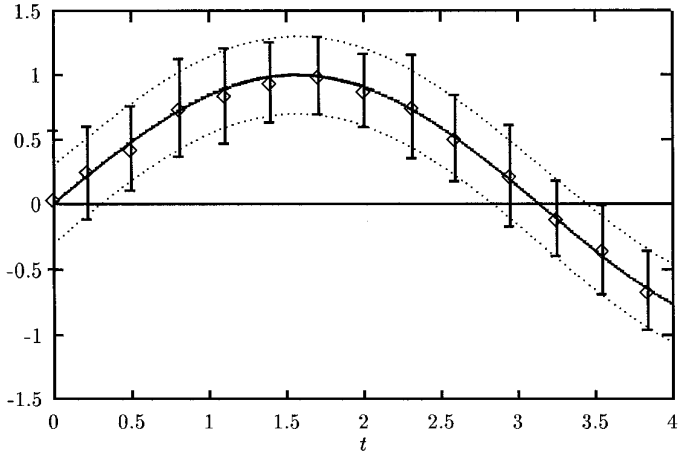

FIG. 9. Same as in Fig. 8 for a parameter value Re = 40. The thickness of the gradient is much smaller than in the Re = 4 case, but the inner subdomain follows the gradient.

TABLE V

Mean Value of the Errors, Defined by Eq. (12), between the Exact Solution and the Computed Solution for the Advection–Diffusion Equation (14) with a Parameter Value Re = 40

$x_{2,\text{interface}}$	Interfaces	u	u'	u''	u'''
1±	Adapted	0.64×10^{-5}	0.14×10^{-1}	0.17×10^{0}	0.92×10^{0}

Note. The jumps of the derivatives are larger than the Re = 4 case.

3.1. *Basic Equations*

The evolution equations for a compressible, viscous, thermally conducting gas with two components of molecular weights m_1 and m_2 are

$$\frac{\partial \rho}{\partial t} + \frac{\partial \rho u_j}{\partial x_j} = 0, \tag{19}$$

$$\left(\frac{\partial}{\partial t} + u_j \nabla_j\right) u_i = -\frac{A_u}{\rho} \nabla_i P + \frac{B_u}{\rho} \nabla_j \sigma_{ij} + C_u \delta_{i2}, \tag{20}$$

$$\left(\frac{\partial}{\partial t} + u_i \nabla_i\right) E = -\frac{A_T}{\rho} \frac{\partial}{\partial x_i} u_i P + \frac{B_T}{\rho} \Delta T + \frac{C_T}{\rho} \nabla_i \sigma_{ij} u_j, \tag{21}$$

$$\left(\frac{\partial}{\partial t} + u_j \nabla_j\right) c = \frac{B_c}{\rho} \Delta c, \tag{22}$$

where the total energy E is defined by

$$E = \frac{1}{2} A_E (u_1^2 + u_2^2) + B_E \frac{C_v}{C_{vr}} T - C_E x_2 \tag{23}$$

and σ_{ij} is the stress tensor,

$$\sigma_{ij} = \left(\frac{\partial u_i}{\partial x_j} + \frac{\partial u_j}{\partial x_i} - \frac{2}{3} \delta_{ij} \frac{\partial u_\ell}{\partial x_\ell}\right), \tag{24}$$

TABLE VI

Same Simulations as in Table V but for the Local Error, ERR, Defined by Eq. (13) Which Characterizes the Jump of the Function and Its Derivatives between Two Subdomains

$x_{2,\text{interface}}$	Interfaces	u	u'	u''	u'''
±0.1	Adapted	0.00	0.29×10^{-8}	0.12×10^{0}	0.40×10^{0}
		0.00	0.50×10^{-7}	0.28×10^{0}	0.40×10^{0}

Note. The upper line refers to the interface between subdomains 1 and 2. The lower one refers to the interface between subdomains 2 and 3.

and $i, j, \ell = 1, 2$. The Stokes relation between the first and second viscosity coefficients has been used. This set of equations is closed by the equation of state for the monatomic perfect gas,

$$P = (1 + r - 2rc)\rho T. \tag{25}$$

In these equations P, ρ, T, and c are the pressure, the density, the temperature, and the concentration, respectively; the u_i are the components of the velocity. The thermal conductivity and the dynamic viscosity coefficients are assumed to be constant. The specific heat at constant volume is $C_v = cC_{v_1} + (1 - c)C_{v_2}$ and $r = (m_1 - m_2)/(m_1 + m_2)$ and $C_{vr} = C_v(c = 0.5)$. The boundary conditions for the velocity, the temperature, and the concentration may be either of Dirichlet or Neumann type. The particular choice will be specified for each numerical application. No boundary conditions are applied on the density and the pressure. In the following, we shall deal with two different instabilities and it is convenient to write the equations into a generic dimensionless form. The coefficients appearing in Eqs. (19)–(23) shall be specified later on. The diffusive parts of the Navier–Stokes are handled implicitly which leads to elliptic problems for the velocity, the temperature, and the concentration. Since the transport coefficients are assumed to be constant, these two-dimensional problems reduce to one-dimensional problems in Fourier space [26].

3.2. *The Parabolic Equations of Velocity, Temperature, and Concentration*

The present work on domain decomposition takes the classical view of the differential equation. For an equation of order d, the function and its derivatives of order up to $d - 1$ must be matched. Consequently, for parabolic problems, both the solution and its first normal derivative must be matched. Several solution techniques are available (for a review, see [1]). The choice of the influence matrix technique has been made since it is a noniterative method. Such a technique has been introduced in the domain decomposition framework by [27] and generalized by [28, 29]. Since all diffusive terms in the full Navier–Stokes equations are nonlinear, they are separated into two contributions as

$$\frac{1}{\rho}\frac{\partial \sigma_{ij}}{\partial x_j} = \left(\frac{1}{\rho} - \frac{1}{\rho_s}\right)\frac{\partial \sigma_{ij}}{\partial x_j} + \frac{1}{\rho_s}\frac{\partial \sigma_{ij}}{\partial x_j}, \tag{26}$$

where $\rho = \rho(x_1, x_2, t)$ and $\rho_s = \rho_s(x_2)$ which does depend upon the x_2-coordinate and thus may be close to the total density. The quantity ρ_s is the mean value, in the x_1-direction, of the total density. The difference between the total density ρ and the mean value ρ_s is only due to the variation of density in the x_1-direction. The first term of the right-hand side of Eq. (26) is treated explicitly while the second one is handled implicitly. This splitting has been suggested in [30] and used by several authors (see, for example, [2]).

The influence matrix method is applied to the temperature, the concentration, and to the two components of the velocity. The idea of the method is to seek the solution as a linear combination of the solution of the homogeneous part of the equation of interest and the solution of the inhomogeneous part. This one uses homogeneous Dirichlet boundary conditions, whereas the homogeneous equations require inhomogeneous boundary conditions. However, any type of physical boundary conditions may be used on the initial equations owing to the linear combination. In the present case, the method is generalized as follows for the two components of the velocity. Since the transport coefficients are constant, the two-dimensional elliptic problems are written in Fourier space. In this space, they are split in N_{x_1} one-dimensional elliptic problems depending upon the wavenumber k. More precisely, the solution is decomposed in Fourier space as

$$\begin{aligned} &\vec{u}_k^{\,m} = \vec{\overline{u}}_k^{\,m} + \sum_{p=1}^{4} \lambda_{p,k}^m \vec{u}_{p,k}^{\,m} \quad \text{for } m = 1, ..., M; \\ &k = -N_{x1}/2, ..., N_{x1}/2 + 1, \end{aligned} \tag{27}$$

with the boundary conditions

$$\alpha_{\vec{u}}\vec{u}_k + \beta_{\vec{u}}\frac{d\vec{u}_k}{dx_2} = 0 \quad \text{at } x_2 = x_{2,\text{inf}}, x_{2,\text{sup}}, \tag{28}$$

where $\alpha_{\vec{u}}$ and $\beta_{\vec{u}}$ are four constants which define the boundary conditions. The quantities $\overline{u}_{1,k}^m$ and $\overline{u}_{2,k}^m$ are solution of the inhomogeneous elliptic problems

$$\begin{aligned} &\frac{d^2\overline{u}_{1,k}^m}{dx_2^2} - \sigma_{1,k}\overline{u}_{1,k}^m - \kappa_{1,k}\frac{d\overline{u}_{2,k}^m}{dx_2} = S_{u_{1,k}}, \\ &x_2 \in \Omega^m, m = 1, ..., M, \\ &\frac{d^2\overline{u}_{2,k}^m}{dx_2^2} - \sigma_{2,k}\overline{u}_{2,k}^m - \kappa_{2,k}\frac{du_{1,k}^m}{dx_2} = S_{u_{2,k}}, \\ &k = -N_{x1}/2, ..., N_{x1}/2 + 1, \end{aligned} \tag{29}$$

with homogeneous Dirichlet boundary conditions

$$\begin{aligned} &\overline{u}_{j,k}^m(x_{2,m-1}) = 0, \quad \overline{u}_{j,k}^m(x_{2,m}) = 0, \\ &m = 1, ..., M \text{ with } j = 1, 2. \end{aligned} \tag{30}$$

Each elementary solution $\vec{u}_{p,k}^{\,m}$ satisfies the following system of equations, in each subdomain,

$$\frac{d^2u^m_{1,p,k}}{dx_2^2} - \sigma_{1,k}u^m_{1,p,k} - \kappa_{1,k}\frac{du^m_{2,p,k}}{dx_2} = 0,$$
$$x_2 \in \Omega^m, m = 1, ..., M-1,$$
$$\frac{d^2u^m_{2,p,k}}{dx_2^2} - \sigma_{2,k}u^m_{2,p,k} - \kappa_{2,k}\frac{du^m_{1,p,k}}{dx_2} = 0, \quad (31)$$
$$k = -N_{x1}/2, ..., N_{x1}/2 + 1,$$

with inhomogeneous Dirichlet boundary conditions

$$u^m_{1,p,k}(x_{2,m-1}) = \delta_{1p}, \quad u^m_{1,p,k}(x_{2,m}) = \delta_{2p}, \quad \text{with } m = 1, ..., M,$$
$$u^m_{2,p,k}(x_{2,m-1}) = \delta_{3p}, \quad u^m_{2,p,k}(x_{2,m}) = \delta_{4p}, \quad (32)$$

where the index p is the number of the elementary solution. The coefficients $\lambda^m_{p,k}$ are obtained as solutions of the matching equations, i.e., the matching of the function and its normal derivative, and the physical boundary conditions

$$u^m_{j,k}(x_{2,m}) = u^{m+1}_{j,k}(x_{2,m}),$$
$$\text{for } m = 1, ..., M-1 \text{ with } j = 1, 2, \quad (33)$$
$$\frac{du^m_{j,k}}{dx_2}(x_{2,m}) = \frac{du^{m+1}_{j,k}}{dx_2}(x_{2,m}),$$
$$\text{for } k = -N_{x1}/2, ..., N_{x1}/2 + 1,$$

$$\alpha_{\text{inf}}u^1_{j,k}(x_{2,\text{inf}}) + \beta_{\text{inf}}\frac{du^1_{j,k}}{dx_2}(x_{2,\text{inf}}) = 0, \quad (34)$$

$$\alpha_{\text{sup}}u^M_{j,k}(x_{2,\text{sup}}) + \beta_{\text{sup}}\frac{du^M_{j,k}}{dx_2}(x_{2,\text{sup}}) = 0.$$

Each of the Eqs. (33) gives $4M - 4$ equations for the $\lambda^m_{p,k}$'s. Equations (34) give four more equations so that the total number of equations is $4M$. The solution provides the $\lambda^m_{p,k}$'s that allows us to build the solution in each subdomain through Eq. (27).

3.3. *The Hyperbolic Equation of Density*

The matching of the density may be done in several ways [1]. Here, a simple procedure has been used, based on the characteristic conditions. The value of the density at the interface is an average of the two values on each side of the interface. More precisely, the procedure reads

$$\rho(x_{2,m}) = \begin{cases} \theta\rho_m(x_{2,m}) + (1-\theta)\rho_{m-1}(x_{2,m}) \text{ if } u_2(x_{2,m}) < 0 \\ (1-\theta)\rho_m(x_{2,m}) + \theta\rho_{m-1}(x_{2,m}) \text{ if } u_2(x_{2,m}) \geq 0, \end{cases} \quad (35)$$

where $m = 1, ..., M-1$.

We shall see below that this formula is mainly used with $\theta = 1$, which means that the density is taken from the upstream subdomain, depending on the normal velocity direction.

3.4. *The Temporal Scheme*

The temporal discretization is the third-order, low storage, semi-implicit Runge–Kutta scheme [1, 31]. All diffusive terms are handled implicitly in Fourier space by means of the Chebyshev acceleration method according to [26]. The time step is subject to the stability condition

$$\Delta t = \text{Min}\left\{ \alpha_{\text{CFL}}\frac{\Delta x_1}{c_s + |u_1|}, \alpha_{\text{CFL}}\frac{\pi\Delta x_2}{c_s + |u_2|}, \alpha_{\text{DIF}}\frac{\Delta x_2^2}{B_{(u,T,c)}(\rho_s/\rho - 1)}\right\}, \quad (36)$$

where Δx_i is the spatial step in the ith direction, c_s is the local sound speed, and α_{CFL} and α_{DIF} are two parameters. The two first constraints correspond to the convective terms which are treated explicitly. The third one is due to the nonlinear diffusion terms also handled explicitly. However, in the numerical simulations reported below, this term is less restricting than the stability condition due to convection. This happens because the mean density ρ_s is closed to the total density. Simulations are usually carried out with α_{CFL} in the range 0.50–0.75 and α_{DIF} equal to 0.5.

4. NUMERICAL APPLICATIONS

4.1. *The Kelvin–Helmholtz Flow*

This flow has received much attention in the last few years, due to its application in industrial projects. Direct numerical simulations have been carried out using either finite-difference type methods or spectral methods [9]. The method used in this reference has been detailed in the Introduction. It is based on a Fourier–Chebyshev expansion and an adaptive mapping in the vertical direction. We present in this section some simulations of the Kelvin–Helmholtz flow carried out with the domain decomposition method previously described. From a numerical point of view, the interest comes from the presence of large gradients of horizontal velocity, in addition to the unsteady character of this configuration. The basic state is found by assuming, as in the boundary layer approximation, that the pressure and the total enthalpy are constant with a Prandtl number equal to one. The units of velocity and length are given by the difference of velocities across the layer $2u_\infty$ and the initial vorticity thickness δ_i. The units of density and temperature are given by the values in the free stream ρ_∞ and T_∞, respectively:

TABLE VII

Characteristics of the Kelvin–Helmholtz Unsteady Solutions

Run	N_d	N_i	N_{x_1}	Interfaces	L_{x_2}	Re	Mach	λ_1	λ_2	λ_3
1	3	3×51	72	Fixed	± 25	400.	0.8	20.000	—	—
2	3	3×51	72	Adapted	± 25	400.	0.8	20.000	—	—
3	7	7×51	100	Adapted	± 25	400.	0.4	17.952	$\lambda_1/3$	—
4	7	7×51	100	Adapted	± 25	400.	0.4	17.952	$\lambda_1/3$	$\lambda_1/2$

Note. The Prandtl number and the ratio of specific heats are equal to 1 and 1.4, respectively.

$$\overline{u}_1 = \tfrac{1}{2}\tanh 2x_2, \quad \overline{u}_2 = 0,$$
$$\overline{T} = 1 + \frac{\gamma - 1}{2} M_\infty^2 (1 - (2\overline{u}_1)^2), \quad \overline{P} = 1. \tag{37}$$

The dimensionless coefficients of the Navier–Stokes equations (19)–(21) are given in Table VIII. The boundary conditions are of Neumann type for the horizontal velocity and the temperature. Dirichlet boundary conditions are applied on the vertical velocity. They read

$$\frac{\partial u_1}{\partial x_2} = 0, \quad u_2 = 0, \quad \frac{\partial T}{\partial x_2} = 0, \quad \text{at } x_2 = \pm L_{x2}. \tag{38}$$

There are no boundary conditions on the density and the pressure. The collocation point generation is performed through the functional (4), based on the quantity $u_1/u_{1,\max}$, where $u_{1,\max}$ is the maximum of the velocity u taken over the two-dimensional domain. This functional is then averaged in the x_1-direction. Mapping (6) is used in each subdomain. The dynamical generation of collocation points and the rezoning of all variables take 12 s on a CRAY-YMP computer for three subdomains with 51 Chebyshev points and 72 Fourier points. The perturbations are written in the general form

$$u_1' = \frac{\varepsilon x_2}{20\pi} \exp\left(-\frac{x_2^2}{10}\right) \sum_{q=1}^{Q} \lambda_q \sin\left(\frac{2\pi x_1}{\lambda_q}\right),$$
$$u_2' = \frac{\varepsilon}{2} \exp\left(-\frac{x_2^2}{10}\right) \sum_{q=1}^{Q} \cos\left(\frac{2\pi x_1}{\lambda_q}\right). \tag{39}$$

Four simulations of the Kelvin–Helmholtz flows have been carried out. Their characteristics are summarized in Table VII. The two first lines correspond to the test case run by Guillard *et al.* [9] with an adaptive procedure in a single domain. The first simulation is carried out with fixed interfaces. The second one uses the moving interface procedure. Both results are compared with the single domain results of [9] in Fig. 10 and Table IX. Figure 10 shows an excellent agreement on global quantity such as the vorticity thickness. This one is defined by

$$\delta_\omega^{-1} = \delta_i^{-1} \frac{\partial}{\partial x_2} \left(\frac{\overline{\rho u_1}}{\overline{\rho}}\right)\bigg|_{\max}, \tag{40}$$

where δ_i is the initial vorticity thickness. The comparison between extreme values of the potential vorticity and the density is given in Table IX. Although the vorticity thicknesses are very closed to each other, the maxima of the potential vorticity differ by 10% at time $t = 40$. The discrepancy on the density between the two numerical methods is less than 0.5%. One conclusion of these runs is that the dynamical generation of collocation points is not necessary in this case.

As an illustration of the robustness of the numerical method, two simulations with a multimode perturbation have been carried out (runs 3 and 4 of Table VII). The wavelengths of the perturbations are determined from the dispersion curve. This one has been obtained with a linear stability code based on the method of normal modes.

TABLE VIII

Dimensionless Coefficients of the Navier–Stokes Equations for the Kelvin–Helmholtz Flow

A_u	B_u	C_u	A_T	B_T	C_T	A_E	B_E	C_E	B_c
$\frac{1}{4\gamma M_\infty^2}$	$\frac{1}{\mathrm{Re}}$	0	$\frac{\gamma - 1}{\gamma}$	$\frac{1}{\sigma \mathrm{Re}}$	$(\gamma - 1)\frac{4M_\infty^2}{\mathrm{Re}}$	$\frac{A_T}{A_u}$	$\frac{1}{\gamma}$	0	0

TABLE IX

Comparison of the Extreme Values of the Potential Vorticity and the Density at Time $t = 40$

Run		Interfaces	ω_{min}	ω_{max}	ρ_{min}	ρ_{max}
	Single domain	—	−0.54910	0.10950×10^{-1}	0.65798	1.2014
1	SECOMD	Fixed	−0.55841	0.98236×10^{-2}	0.65530	1.2008
2	SECOMD	Adapted	−0.55944	0.10191×10^{-1}	0.65043	1.2043

Note. The first line refers to the adaptive single domain numerical method developed by Guillard *et al.* The results of the second line have been obtained with the present multidomain method with fixed interfaces whereas the last line has been obtained with the dynamical generation of collocation points (SECOMD).

The dispersion curve corresponding to the parameter values of runs 3 and 4 is displayed in Fig. 11. From this curve two modes of equal growth rate are determined in such a way that $\lambda_2 = \lambda_1/3$. In run 4 the most dangerous mode whose wavelength is $\lambda_1/2$ has been added.

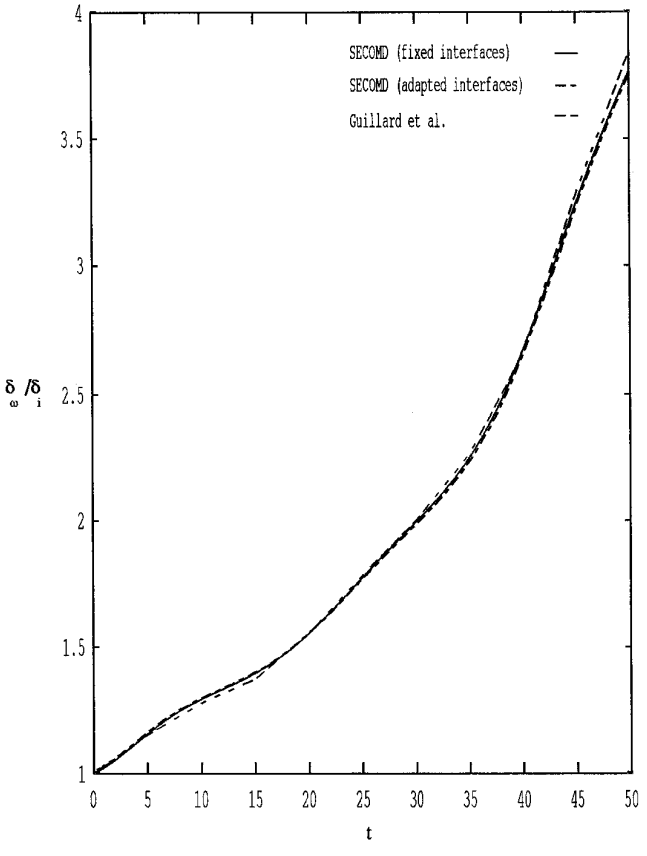

FIG. 10. Vorticity thicknesses obtained with the present multidomain technique (called SECOMD) with fixed interfaces and by using the dynamical generation of collocation points. The third result has been obtained with the single domain adaptive spectral code of Guillard *et al.* The two first results are almost superposed. The third one is very close to the SECOMD result.

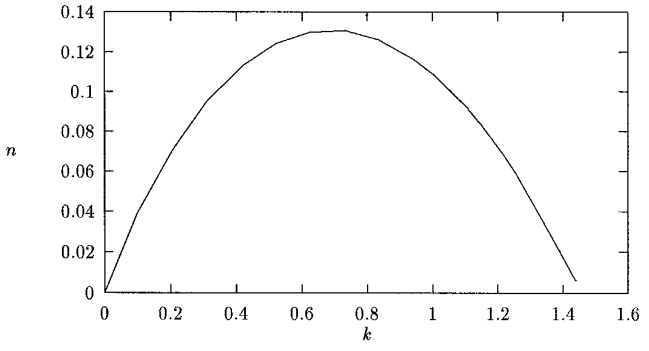

FIG. 11. Dispersion curve of the temporal two-dimensional Kelvin–Helmholtz instability. The growth rate and the wavenumber are noted n and k, respectively. The convective Mach number is 0.4 and the Reynolds number is 400. The Prandtl number and the ratio of specific heats are equal to 1 and 1.4, respectively.

The two-mode run uses seven subdomains with 51 Chebyshev collocation points on each and 100 Fourier points on the horizontal direction. Since both the solution and the best location of the subdomains are not known at the beginning of the computation, the same number of Chebyshev collocation points have been used in each subdomain. Figure 12 shows the three vortices at the very beginning of the simulation. From time $t = 25$ to $t = 50$ they are rolling over each other. The pairing process is completed at $t = 55$. The pairing between the resulting vortex and the initial third one begins at $t = 50$. At $t = 105$ the pairing is completed. The interfaces between subdomains are localized at $x_2 = 16.0$, 5.47, and 1.15 at time $t = 35$ and at $x_2 = 17.2$, 8.67, and 1.55 at time $t = 105$. Since the flow is almost symmetric with respect to the origin, the interfaces are constrained to be also symmetric. At that time the gradients have been smoothed and consequently the central subdomain is larger. It is worthwhile to note that the interfaces are located inside the main vortex where the physical quantities and their derivatives have nonnegligible values.

The three-mode run uses the same spatial discretization as the two-mode run ($7 \times 51 \times 100$). The results of this simulation are presented in Fig. 13. According to linear stability theory, the most dangerous mode produces the vortex that grows faster in time. Very quickly, the first pairing process is completed. At $t = 35$ the second one begins and ends at $t = 55$. Afterwards, this is simply the evolution of one vortex of which decays very slowly in time. The isocontours of the production term $\vec{\nabla}\rho \times \vec{\nabla}P$ of the vorticity equation have been plotted, from both the two- and three-mode simulations, but they are not presented here. They do not display any defect at the numerical interfaces. Of course, this term is not the dominant vorticity production in a Kelvin–Helmholtz instability. However, it is interesting to check this point since neither

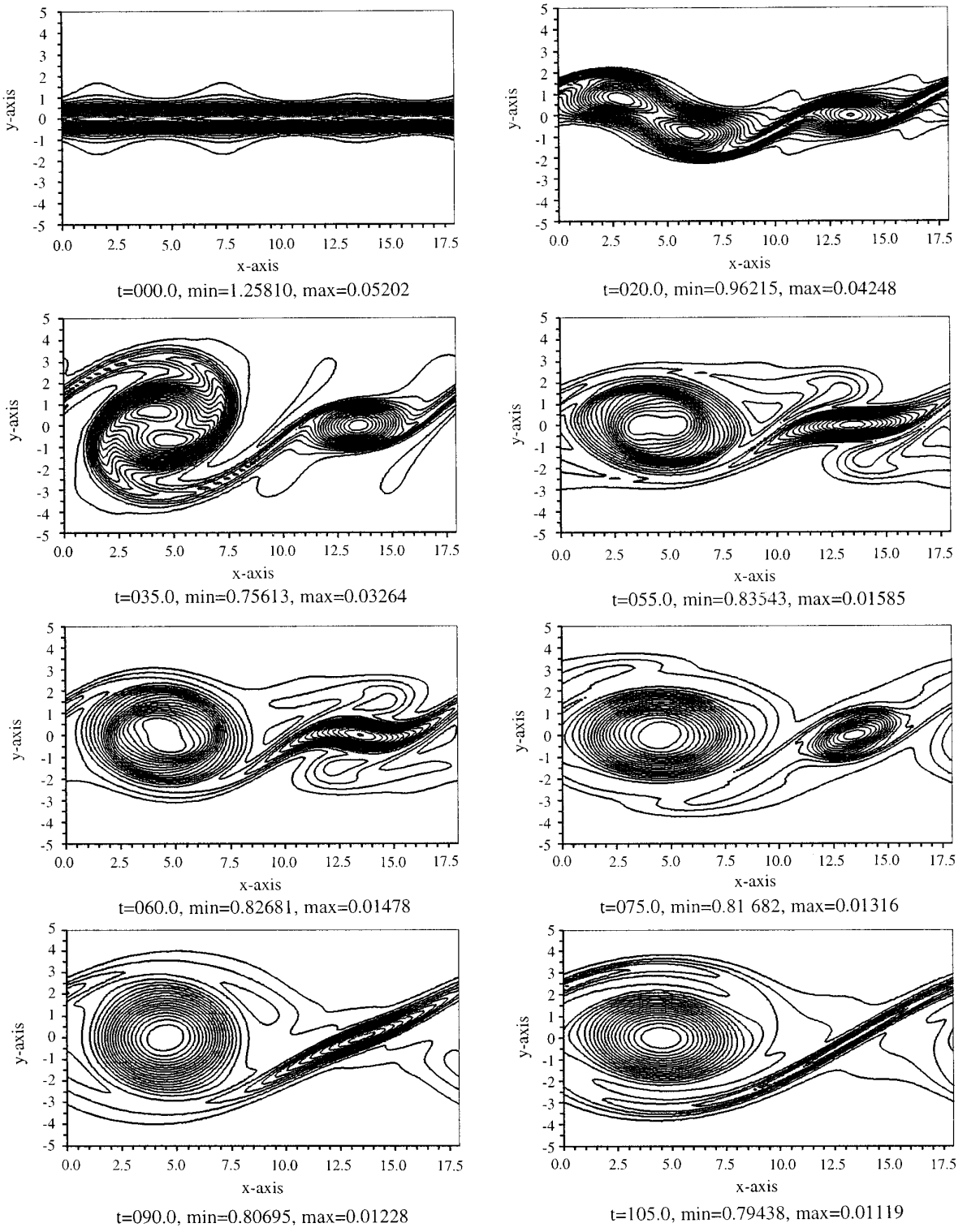

FIG. 12. Potential vorticity at selected times in the two-mode simulation. The minimum of this quantity is given in each picture.

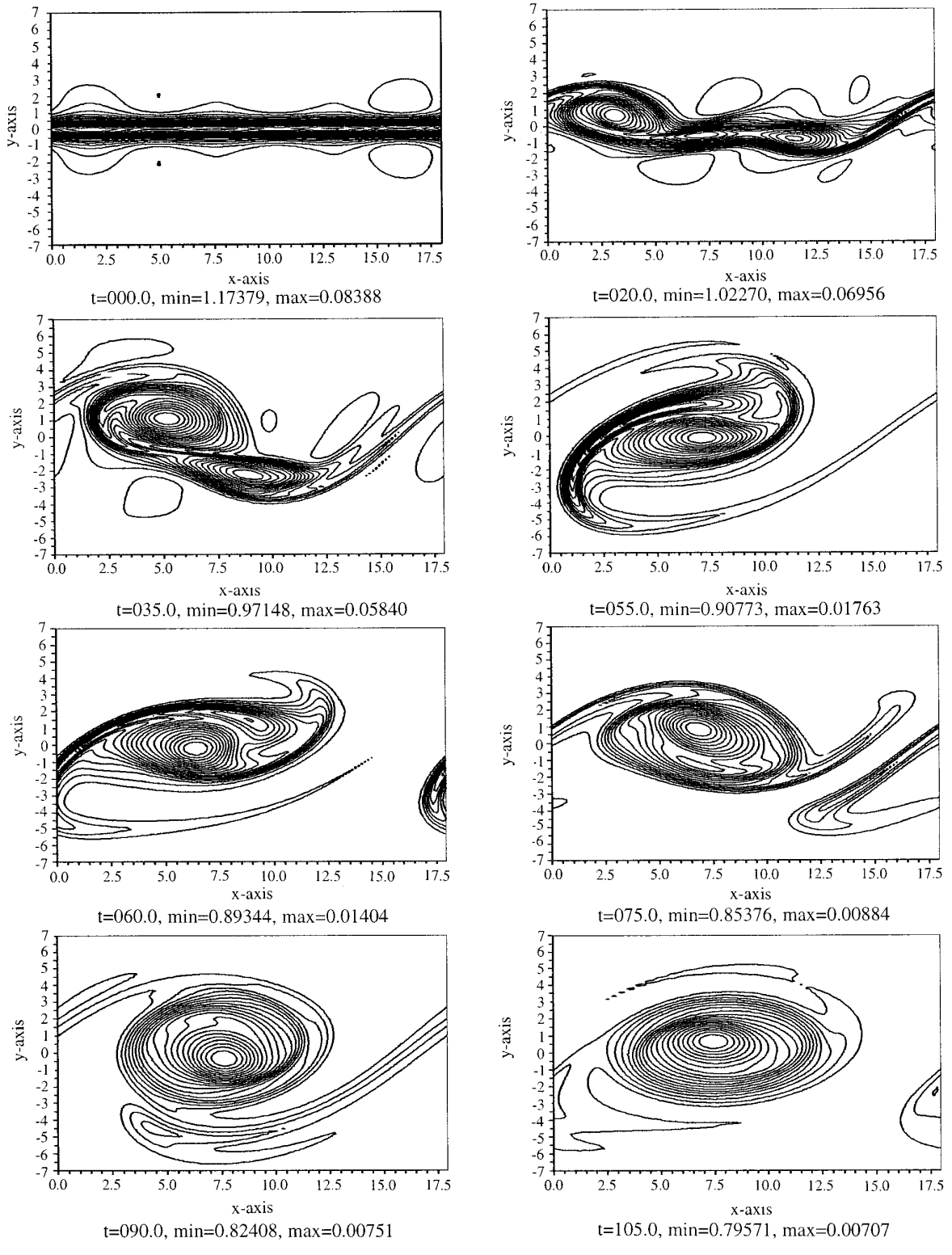

FIG. 13. Potential vorticity at selected times in the three-mode simulation. The minimum of this quantity is given in each picture.

TABLE X

Dimensionless Coefficients of the Navier–Stokes Equations for the Rayleigh–Taylor Flow

A_u	B_u	C_u	A_T	B_T	C_T	A_E	B_E	C_E	B_c	r
$\frac{1}{\gamma M^2}$	$\frac{1}{8\pi^2}$	$\frac{1}{\pi A_t}$	$\frac{\gamma-1}{\gamma}$	$\frac{1}{8\pi^2\sigma}$	$(\gamma-1)\frac{M^2}{8\pi^2}$	$\frac{A_T}{A_u}$	$\frac{1}{\gamma}$	$\frac{A_T C_u}{A_u}$	$\frac{1}{8\pi^2 Sc}$	A_t

the continuity of the derivative of the density nor the pressure are enforced in the matching conditions. We also check that these flows cannot be simulated without the dynamical generation of collocation points. Indeed, in a fixed interface calculation spurious oscillations appear at the numerical interfaces. These oscillations grow with time and diffuse all over the two-dimensional domain.

4.2. *The Rayleigh–Taylor Flow*

The Rayleigh–Taylor instability may occur in configurations in which a fluid supports a denser fluid against gravity. This flow is the object of a continuing interest due to its application to inertial confinement fusion [32]. We present in this section one simulation of this flow. From a numerical point of view, the interest comes from the presence of quasi-discontinuous density and concentration profiles and from the unsteady character of the solution. The linear stability analysis of the Rayleigh–Taylor flow with two viscous diffusive compressible fluids has not been solved. Instead, we will use the approximate dispersion law given by Duff *et al.* [33] in which both components of the incompressible fluid have the same constant kinematic viscosity ν and diffusion coefficient D. It reads

$$n = \sqrt{A_t g k + \nu^2 k^4} - (\nu + D)k^2, \tag{41}$$

where A_t, g, and k are the Atwood number, the gravity acceleration, and the wavenumber, respectively. This curve has a maximum defined by

$$k_{\max} = \frac{2\pi}{\lambda_{\max}} = \frac{1}{2}\left(\frac{A_t g}{\nu^2}\right)^{1/3}, \quad n_{\max} = \frac{1}{2}\left(\frac{A_t^2 g^2}{\nu}\right)^{1/3}, \tag{42}$$

for vanishing diffusion coefficient, where $k_{\max}$ and $n_{\max}$ are the wavenumber and the growth rate of this maximum. These quantities provide the units of length and time. The units of density and temperature are the values at the middle of the central gradient initially located at the origin of the x_2 coordinate, i.e., $\rho(x_2 = 0)$ and $T(x_2 = 0)$, respectively. The dimensionless coefficients of the Navier–Stokes equations (19)–(24) are given in Table X. The Prandtl number is σ, the Mach number is defined by $M = \lambda_{\max} n_{\max}/c_s$, where c_s is the speed of sound, and $Sc = \nu/D$ is the Schmidt number.

The basic state is found by assuming the hydrostatic equilibrium in the upper and lower fluids, with a constant temperature. Since spectral methods do not like discontinuities, the density profile is smoothed by using the function $\mathrm{H}_{\pm}(x_2) = 1 \pm \mathrm{erf}(x_2/\delta)$. The temperature profile is then found by solving the energy equation (21). It becomes

$$\begin{aligned}
\overline{\rho} &= \tfrac{1}{2}(1 - A_t)\exp(A_+ x_2)\mathrm{H}_-(x_2) + \tfrac{1}{2}(1 + A_t)\exp(A_- x_2)\mathrm{H}_+(x_2) \\
\overline{c} &= \tfrac{1}{2}(1 + A_t)\exp(A_- x_2)\mathrm{H}_+(x_2)/\overline{\rho} \\
\overline{T} &= \tfrac{1}{2}(1 - A_t^2)[\exp(A_+ x_2)\mathrm{H}_+(x_2) + \exp(A_- x_2)\mathrm{H}_-(x_2) \\
&\quad - \exp(A_+^2\delta^2/4)\mathrm{H}_+(x_2 - A_+\delta^2/2) \\
&\quad + \exp(A_-^2\delta^2/4)\mathrm{H}_+(x_2 - A_-\delta^2/2)]/\overline{\rho}(1 + A_t - 2A_t\overline{c}),
\end{aligned} \tag{43}$$

where $A_{\pm} = \gamma M^2/(\pi A_t(1 \pm A_t))$ and $\mathrm{H}_{\pm}(x_2) = 1 \pm \mathrm{erf}(x_2/\delta)$. The parameter δ represents the width of the central gradient of the density. A single mode perturbation is introduced in the density and concentration profiles

$$\rho(x_1, x_2) = \rho\left(x_2 - \varepsilon\cos\left(\frac{2\pi x_1}{\lambda}\right)\exp(-10x_2^2)\right) \tag{44}$$

$$c(x_1, x_2) = c\left(x_2 - \varepsilon\cos\left(\frac{2\pi x_1}{\lambda}\right)\exp(-10x_2^2)\right), \tag{45}$$

where ε and λ are the amplitude and the wavelength of the perturbation, respectively. The wavelength corresponds to the maximum growth rate of the linear stability theory. The dimensionless form of the dispersion relation (41) reads

$$n^* = \frac{1}{2}\sqrt{k^{*4} + 8k^*} - \frac{1}{2}\left(1 + \frac{1}{Sc}\right)k^{*2}, \tag{46}$$

where $n^* = n/n_{\max}$ and $k^* = k\lambda_{\max}/2\pi$. The wavenumber which corresponds to the maximum growth rate is

$$k^*_{\max} = \frac{2\pi}{\lambda^*_{\max}}\left(\frac{2(Sc^2 + 4Sc + 2)}{2Sc + 1}\left(\sqrt{1 + \frac{2Sc^3 + Sc^2}{(Sc^2 + 4Sc + 2)^2}} - 1\right)\right)^{1/3}. \tag{47}$$

For vanishing molecular diffusion, the Schmidt number goes to infinity and we obtain $k^* = 1$, as expected. The numerical simulation is defined by the following parameter values:

$$M = 0.3, \quad A_t = 0.4, \quad Sc = 1, \quad \lambda^*_{\max} = 1.9225,$$
$$\delta = 0.06, \quad \varepsilon = 0.1, \quad \sigma = 0.71, \quad \gamma = 1.4.$$

It uses five subdomains with 51 Chebyshev points in each one and with 120 Fourier points in the horizontal direction. As opposed to the Kelvin—Helmholtz simulations, the locations of the interfaces are not constrained to be symmetric with respect to the origin, except at the boundaries of the inner most subdomain. The computational domain is $[0, \lambda_{\max}] \times [-7, 10]$. In the vertical direction, the boundary conditions are of Dirichlet type for the vertical velocity and of Neumann type for the horizontal velocity, the temperature, and the concentration. The generation of collocation points is performed through the functional (4), based on the quantity

$$u = \frac{u_1}{u_{1,\max}} + \frac{u_2}{u_{2,\max}} + \frac{c}{c_{\max}} + \frac{T}{T_{\max}}, \tag{48}$$

where the maximum of each quantity is taken over the two-dimensional domain. This functional is then averaged in the x_1-direction. Mapping (6) has been used in each subdomain. We also carried out a simulation with the same parameter values but with fixed interfaces. Some spurious oscillations appear at the numerical interfaces very quickly in time. Then these oscillations diffuse all over the two-dimensional domain. This shows that moving interfaces are necessary to handle this configuration. In Fig. 14, the initial density profile at $x_1 = \lambda_{\max}/2$ is plotted versus the x_2 coordinate. A zoom in of the concentration profile is given in Fig. 15. It shows that the central gradient is almost a discontinuity (the thickness of the gradient is equal to 10% of the perturbation wavelength and it is less than 1% of the size of the computational domain). Nevertheless, the numerical method can handle these stiff gradients. The simulation has been carried out up to time $t = 10$ which is more than seven times the dimensionless linear characteristic growth time. Figure 16 displays the isocontours of concentration at time $t = 10$. We recognize the mushroom like structure. However, the classical Kelvin–Helmholtz vortices on each side of the mushroom are inhibited by diffusion. Indeed, the horizontal gradient of the vertical velocity is smoothed by diffusion. This structure lies over three subdomains. The interfaces are located at $x_2 = -5.43$, -1.17, 1.17, and 2.60 at time $t = 5.4$ and at $x_2 = -3.33$, -1.11, 1.11, and 4.85 at time $t = 10$.

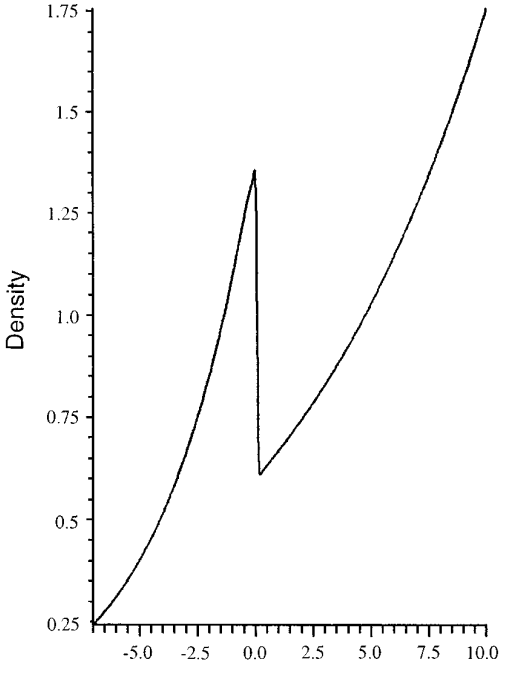

FIG. 14. Density profile given by the first of Eq. (43). The Mach number is $M = 0.3$, the Atwood number is $A_t = 0.4$, and the ratio of the specific heats is $\gamma = 1.4$. The gravity goes from left to right.

5. CONCLUSION

A dynamical pseudo-spectral domain decomposition method has been developed. In each subdomain a transformation of the coordinate that depends on one parameter is used. Both the mapping parameters and the locations of the interfaces are dynamically adapted by minimizing the H^2_ω-norm of the calculated solution. We have shown on simple functions that the total norm depends on the location of these interfaces. The solution of two differential model equations have shown the efficiency of the numerical method to find the best location of the interfaces. The

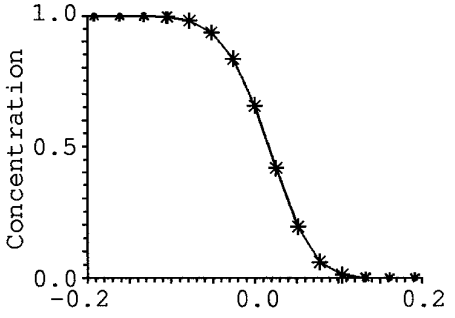

FIG. 15. Zoom in the concentration profile in the vicinity of the central gradient after the first time step and after the procedure of collocation point generation has been applied. The asterisks indicate the collocation points.

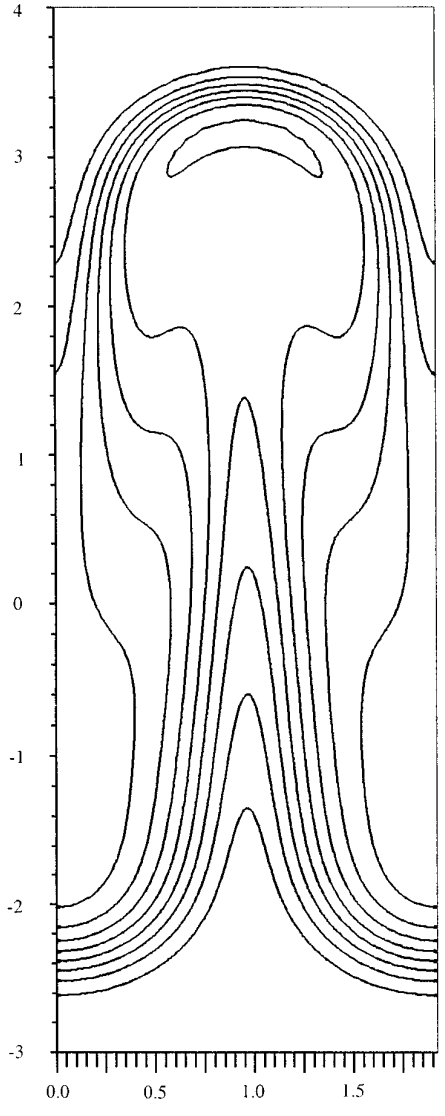

FIG. 16. Isocontours of the concentration at time $t = 10$. The gravity acceleration goes from bottom to top. The light fluid is lying above the heavy fluid. The interfaces are located at $x_2 = -3.33, -1.11, 1.11, 4.85$. The central domain is constrained to be symmetric with respect to the origin.

effect of such a dynamical procedure is to minimize the influence of the initial distribution of the collocation points. It turns out that the overall accuracy is increased. Moreover, it automatically applies without prior knowledge of the location of the rapid variation.

This numerical method has been applied to the simulation of the full Navier–Stokes equations in two dimensions. Matching of the density uses a simple upwind procedure whereas velocity, temperature, and concentration are matched with a method is derived from the influence matrix technique. The method is illustrated on the compressible subsonic viscous Kelvin–Helmholtz and Rayleigh–Taylor flows. This technique of dynamical generation of colloca-

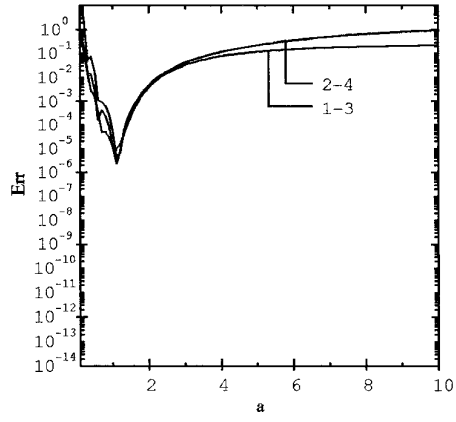

FIG. 17. Comparison of two methods of spectral derivation on the profile $\tanh 2x_2$ in the interval $[-5, 5]$. The error between the computed solution and the exact one is displayed versus the mapping parameter **a**. The number of collocation points is 21. The labels 1 and 2 refer to the first and second derivatives with matrix product, respectively, whereas 3 and 4 refer to the first and second derivatives with the FFT.

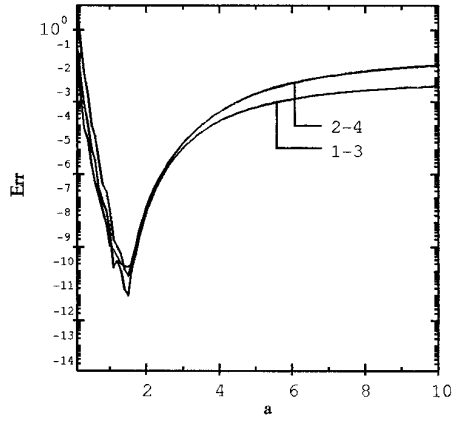

FIG. 18. Same as in Fig. 17 with 51 collocation points.

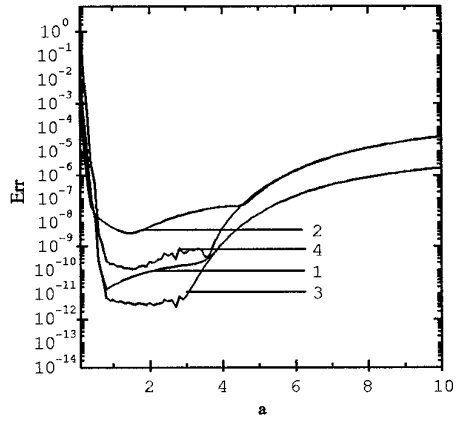

FIG. 19. Same as in Fig. 17 with 101 collocation points.

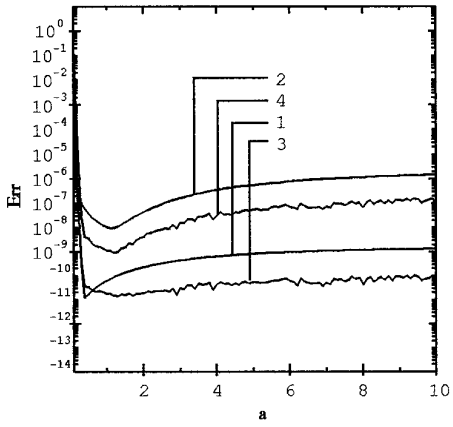

FIG. 20. Same as in Fig. 17 with 201 collocation points.

tion points may be extended to several directions of space. This would allow the numerical simulation of flows with several inhomogeneous dimensions such as the Poiseuille open flow. On the other hand, extension of this method with two periodical directions is straightforward and well suited for the Rayleigh–Taylor instability.

APPENDIX A: DERIVATIVES WITH A TRANSFORMATION OF COORDINATE

In this appendix we compare two methods of derivation of Chebyshev expansion with a coordinate transform. The first one is the matrix multiplication. In this case the second-order derivative operator is obtained by using the square of the first-order operator as recommended by Rothman [34]. The second method is the fast Fourier transform (FFT). The comparison is carried out on the function $\tanh 2x_2$ profile. The error between the computed solution and the exact one are plotted versus the value of the parameter mapping. The results are displayed in Figs. 17–20. The main conclusions are the following ones:

- with 21 and 51 collocation points there is no difference between the two methods. The best accuracy is obtained for a very small domain of values of the parameter mapping.
- the best accuracy obtained with 21 is only 10^{-6} for this particular function. An accuracy of 10^{-11} requires 51 Chebyshev polynomials.
- The FFT method becomes more accurate than the matrix product method for a large number of collocation points (101 and 201). In those cases the differences may reach one or two orders of magnitude.
- For these spatial discretizations, the best accuracy is obtained for a large domain of values of the parameter mapping.

We conclude that the matrix multiplication has to be used only with a relatively small number of collocation points. This point is well known when no mapping is used. When a transformation of coordinates is used with a low order approximation the mapping parameter has to be accurately determined.

APPENDIX B: PROPERTIES OF THE COORDINATE TRANSFORM

In this appendix, we describe the coordinate transform used in this paper. This coordinate transform depends only on the domain boundaries and on one parameter

$$x_2(\zeta) = \frac{x_{2,\mathrm{inf}} + x_{2,\mathrm{sup}}}{2} + \mathbf{a}\zeta \Bigg/ \sqrt{1 + \left(\frac{2\mathbf{a}}{x_{2,\mathrm{sup}} - x_{2,\mathrm{inf}}}\right)^2 - \zeta^2},$$
$$x_2 \in [x_{2,\mathrm{inf}}, x_{2,\mathrm{sup}}],\ \zeta \in [-1, 1],\ \mathbf{a} > 0. \tag{49}$$

For small values of the parameter **a**, this mapping concentrates the collocation points around the middle of the domain $(x_{2,\mathrm{sup}} + x_{2,\mathrm{inf}})/2$. For very large values of the parameter **a**, mapping (49) leads to the Gauss–Lobatto distribution of collocation points. Then, there must exist a value of the parameter **a** that corresponds to a quasi-uniform distribution of the collocation points. This value depends only on the ratio $2/(x_{2,\mathrm{sup}} - x_{2,\mathrm{inf}})$ and is obtained by minimizing the quantity

$$\Delta(N) = 2/(x_{2,\mathrm{sup}} - x_{2,\mathrm{inf}}) \sum_{j=0}^{N-1} |x_2(\xi_j) - x_2(\xi_{\mathrm{equi},j})|^2 \tag{50}$$

with respect to $2/(x_{2,\mathrm{sup}} - x_{2.\mathrm{inf}})$. One gets the expression

$$\mathbf{a} = 0.3277(x_{2,\mathrm{sup}} - x_{2,\mathrm{inf}}). \tag{51}$$

ACKNOWLEDGMENTS

We thank R. Peyret and H. Guillard for helpful comments and suggestions. We also thank J. M. Malé for having provided to us the software for the adaptive procedure.

REFERENCES

1. C. Canuto, M. Y. Hussaini, A. Quarteroni, and T. A. Zang, *Spectral Methods in Fluids Dynamics* (Springer-Verlag, New York, 1988).
2. T. Passot and A. Pouquet, *J. Comput. Phys.* **75,** 300 (1988).
3. C. E. Grosch and S. A. Orszag, *J. Comput. Phys.* **25,** 273 (1977).
4. A. Bayliss and B. J. Matkowsky, *J. Comput. Phys.* **71,** 147 (1987).
5. H. Guillard and R. Peyret, *Comput. Methods Appl. Mech. Eng.* **66,** 17 (1988).
6. A. Bayliss, D. Gottlieb, B. J. Matkowsky, and M. Minkoff, *J. Comput. Phys.* **81,** 421 (1989).
7. J. M. Augenbaum, *Appl. Numer. Math.* **5,** 459 (1989).
8. J. M. Malé, *Calcul d'écoulements visqueux compressibles par méthodes*

spectrales auto-adaptatives. Application aux couches de mélange, Thèse Université de Nice-Sophia-Antipolis, 1992.

9. H. Guillard, J. M. Malé, and R. Peyret, *J. Comput. Phys.* **102,** 114 (1992).
10. A. Solomonoff and E. Turkel, *J. Comput. Phys.* **81,** 239 (1989).
11. A. Bayliss, R. Kuske, and B. J. Matkowsky, *J. Comput. Phys.* **91,** 174 (1990).
12. D. Kosloff and H. Tal-Ezer, *J. Comput. Phys.* **104,** 457 (1993).
13. A. Bayliss, A. Class, and B. J. Matkowsky, *J. Comput. Phys.* **116,** 160 (1995).
14. R. Peyret, *Comput. Methods Appl. Mech. Eng.* **80,** 129 (1990).
15. D. Sidilkover and G. E. Karniadakis, *J. Comput. Phys.* **107,** 10 (1993).
16. W. S. Don, *J. Comput. Phys.* **110,** 103 (1994).
17. A. Suresh, *J. Comput. Phys.* **114,** 339 (1994).
18. A. Bayliss, T. Belytschoko, D. Hansen, and E. Turkel, Adaptive multi-domain spectral methods, in *Proceedings, 5th SIAM Conference on Domain Decomposition Methods for Partial Differential Equations, 1992,* edited by Keyes, Chan, Meurant, Scrooggs, and Voigt (SIAM, Philadelphia, 1992), p. 195.
19. A. Bayliss, M. Garbev, and B. J. Matkowsky, *J. Comput. Phys.* **119,** 132 (1995).
20. A. T. Patera, *J. Comput. Phys.* **54,** 468 (1984).
21. S. Gauthier, T. Desmarais, and G. Iooss, *Europhys. Lett.* **10,** 543 (1989).
22. S. Gauthier, *J. Comput. Phys.* **75,** 217 (1988).
23. F. Renaud, *Une méthode spectrale de décomposition dynamique de domaines: Applications aux écoulements compressibles de Rayleigh–Bénard et de Kelvin–Helmholtz.,* Thèse, Université de Nice-Sophia-Antipolis, 1996.
24. S. Gauthier and F. Renaud, A spectral domain decomposition technique for viscous compressible flows, in *Proceedings, Third International Conference on Spectral and High Order Methods,* (Houston, Texas, June 5–9, 1995) *Houston J. Math.* **437** (1995).
25. U. Ehrenstein, H. Guillard, and R. Peyret, *Numer. Methods Fluids Dyn.* **9,** 499 (1989).
26. S. Gauthier, *Int. J. Num. Methods Fluids* **12,** 985 (1991).
27. M. G. Macaraeg and C. L. Street, *Appl. Numer. Math.* **2,** 95 (1986).
28. J. P. Pulicani, *Computers & Fluids* **16,** 207 (1988).
29. J. P. Pulicani, *Application des méthodes spectrales à l'étude d'écoulements de convection,* Thèse, Université de Nice, pp. 19–52, 1988.
30. D. Gottlieb and S. A. Orszag, *Numerical Analysis of Spectral Methods: Theory and Applications* (SIAM, Philadelphia, 1977).
31. J. H. Williamson, *J. Comput. Phys.* **35,** 48 (1980).
32. H. J. Kull, *Phys. Rep.* **206,** No. 5, 197 (1991).
33. R. E. Duff, F. H. Harlow, and C. W. Hirt, *Phys. Fluids* **5,** 417 (1962).
34. E. E. Rothman, Reducing round-off error in Chebyshev pseudospectral computations, in *High Performance Computing II, 1991,* edited by M. Durand and F. El Dabaghi (Elsevier Science, Amsterdam, 1991), p. 423.